Earth and Planetary Science Letters 275 (2008) 127–137

Contents lists available at ScienceDirect

Earth and Planetary Science Letters

journal homepage: www.elsevier.com/locate/epsl

Constraining denitrification in permeable wave-influenced marine sediment using linked hydrodynamic and biogeochemical modeling

M. Bayani Cardenas [a,*], Perran L.M. Cook [b], Houshuo Jiang [c], Peter Traykovski [c]

[a] Department of Geological Sciences, University of Texas at Austin, Austin Texas 78712, USA
[b] Water Studies Centre, Monash University, Clayton 3800, Victoria, Australia
[c] Woods Hole Oceanographic Institution, Woods Hole Massachusetts 02543, USA

ARTICLE INFO

Article history:
Received 7 November 2007
Received in revised form 11 August 2008
Accepted 12 August 2008
Available online 23 September 2008

Editor: M.L. Delaney

Keywords:
permeable sediment
oscillatory ripples
computational fluid dynamics
pore water
denitrification
reactive transport

ABSTRACT

Permeable marine sediments are ubiquitous complex environments, the biogeochemistry of which are strongly coupled to hydrodynamic process above and within the sediment. The biogeochemical processes in these settings have global scale implications but are poorly understood and challenging to quantify. We present the first simulation of linked turbulent-oscillatory flow of the water column, porous media flow, and solute transport in the sediment with oxygen consumption, nitrification, denitrification, and ammonification, informed by field- and/or experimentally-derived parameters. Nitrification and denitrification were significantly impacted by advective pore water exchange between the sediment and the water column. Denitrification rates showed a maximum at intermediate permeabilities, and were negligible at high permeabilities. Denitrification rates were low, with only ~15% of total N mineralized being denitrified, although this may be increased temporarily following sediment resuspension events. Our model-estimated denitrification rates are about half of previous estimates which do not consider solute advection through the sediment. Given the critical role of sediment permeability, topography, and bottom currents in controlling denitrification rates, an improved knowledge of these factors is vital for obtaining better estimates of denitrification taking place on shelf sediment. Broad application of our approach to myriad conditions will lead to improved predictive capacity, better informed experimental and sampling design, and more holistic understanding of the biogeochemistry of permeable sediment.

1. Introduction

The continental shelf from the coast to hundreds of kilometers offshore is covered with permeable marine sediment where hydrodynamic and biogeochemical processes occurring above and within the sediment are connected, requiring a shift in how we view and study these settings (Boudreau et al., 2001; Burnett et al., 2003; Huettel et al., 2003). Fluid flow above permeable sediment generates pressure gradients along the sediment–water interface (SWI), driving fluid exchange across it. Oscillatory motion due to waves and tides is enough to generate pressure gradients along a flat SWI, but the gradients become more prominent due to interaction between currents and topographic features such as ripples and biogenic mounds (Webb and Theodor, 1968; Riedl et al., 1972; Thibodeaux and Boyle, 1987; Shum, 1992; Huettel and Gust, 1992; Shum, 1995). This exchange mechanism, that persists from the coast up to areas of the continental shelf that are more than 100 m deep, is sometimes referred to as the "subtidal pump" (Riedl et al., 1972). Advective fluid flux from sediment to the bottom water has been observed as far away as 80 km from the coast (Moore and Shaw, 1998), indicating that the process potentially occurs over a broad section of the continental shelves.

Pumping of bottom water through permeable shelf sediment represents the largest flux of pore water into the ocean, even compared to terrestrially-sourced submarine groundwater discharge (e.g., Moore, 1996; Michael et al., 2005). In fact, recent observations show that the residence time of pore water in the upper few meters of shelf sediment is only a few months (Moore and Wilson, 2005) while global scale computations show that the subtidal pump could flush the entire ocean's volume in as little as 14,000 years (Riedl et al., 1972). It is clear that this exchange process is important for shelf settings across a broad range of spatial and temporal scales. Earlier studies have shown that connections and nutrient fluxes between the continental margins and the deep sea are equally important in material cycling (Walsh, 1991). Coupled fluid and chemical exchange fluxes in permeable sediment potentially play a role in global biogeochemical cycles.

Solute transport rate, biogeochemical reactions and hydrodynamic processes are tightly coupled in permeable sediment. Experiments using flumes have shown that sediment O_2 uptake rates in permeable sediment are strongly influenced by current velocities (Huettel et al., 1998). This effect has also been shown to occur in-situ in benthic

* Corresponding author. Tel.: +1 512 471 6897.
E-mail address: cardenas@mail.utexas.edu (M.B. Cardenas).

0012-821X/$ – see front matter © 2008 Elsevier B.V. All rights reserved.
doi:10.1016/j.epsl.2008.08.016

chambers (Cook et al., 2007) and has been observed with microelectrodes (Werner et al., 2006). Moreover, nitrification and denitrification rates can be substantially affected by pore water advection, with complex interactions between flushing rate and solute concentrations in the overlying water column (Cook et al., 2006). We note that the previous study by Cook et al. (2006) considered artificial flushing conditions within a benthic chamber to mimic natural conditions; further investigation is required to elucidate the impact of flushing on denitrification in natural settings.

Nitrogen is a critical nutrient within the ocean that often limits productivity. Hence, there is much interest in constraining the global nitrogen cycle, that has some major uncertainties at present, particularly in the major sink, denitrification (Codispoti, 2007). Shelf sediment is estimated to account for about a third to a half of benthic global denitrification (Middelburg et al., 1996), yet there are few measurements or models that describe this process in permeable sediment that dominate the continental shelf (Middelburg et al., 1996).

Advancing our fundamental understanding of the biogeochemistry of permeable sediment requires placing equal emphasis on the hydrodynamic processes, especially for rippled seabeds. The ever-expanding computing power and advances in computational fluid dynamics algorithms have allowed for using Large-Eddy Simulation (LES) to fairly accurately simulate turbulent flows over ripples and under waves plus currents (e.g., Zedler and Street, 2001, 2006; Chang and Scotti, 2003, 2004; Barr et al., 2004). A recent LES model developed by Jiang and Traykovski (2006) for application of waves over sandy rippled seabeds makes it possible to use field data, such as observed wave forcing and ripple topography, to drive the model and has achieved quite favorable comparison between model results and field observations.

Shum (1992) modeled fluid flow through rippled sediment forced by progressive gravity waves passing over the sediment. The pressure distribution along a flat SWI was determined by an analytical solution to the oscillatory flow assuming potential flow theory and also by numerically solving the two-dimensional Navier–Stokes equation. The pressure solution, with a high at the crest of an undulating symmetric ripple and a low near the troughs, was then used as a boundary condition for the groundwater flow equation that assumes Darcian flow through the sediment. This results in a flow field where pore water is infiltrated from the troughs and exits back into the overlying water column at the crest. This flow field has been demonstrated many times in laboratory settings (e.g., Precht and Huettel, 2004) and more recently under natural conditions (Cook et al., 2007). Shum later extended his modeling study to include transport through the rippled sediment of a single-reacting solute (oxygen) that follows a first-order consumption rate (Shum, 1993, 1995; Shum and Sundby, 1996). However, Shum's pioneering work did not account for turbulence and assumed that turbulent-oscillatory flow can be represented by potential flow theory. This assumption and simplification is unverified. Recent simulations of coupled channel flow and pore water flow through ripple and dune sediment show drastic differences between cases when turbulence is ignored and when turbulence is considered in the overlying water column (Cardenas and Wilson, 2007a,b; Meysman et al., 2007). Given the lack of representation for turbulence, the modeled flow fields presented previously may look qualitatively similar to reality but may actually be inaccurate quantitatively. Moreover, the previous studies have only considered idealized sinusoidal ripples and simple non-coupled reactions.

Accurate estimates of biogeochemical reactions rates can be achieved via better representation of coupled processes in robust numerical transport models. Reactive transport modeling is expected to lead towards answers to challenging but critical fundamental questions in the Earth sciences (Steefel et al., 2005). Diagenetic models are now mature enough to consider the interactions and kinetics of multiple species (e.g., Soetaert et al., 1996; Van Cappelen and Wang, 1996; Meysman et al., 2003). But most still consider either a one-dimensional (1D) diffusive model ignoring advection, that are perfectly suitable for sediment with low permeability such as muds and clays, or 1D models that represent advection with enhanced diffusivities (Boudreau, 2000). One-dimensional models were partly driven by lack of measurement methods that warranted two-dimensional (2D) explanations, i.e., most chemical measurements were taken along 1D profiles (Boudreau, 2000). Recently, Cook et al. (2006) modeled coupled denitrification processes with 2D advective transport for stirred benthic chambers. To our knowledge, there has been no study that links sufficiently accurate models for turbulent-oscillatory flow over ripples with two-dimensional multi-species reactive transport through the sediment. Given that a vast area of the continental shelf is subjected to these processes, high-fidelity quantitative modeling of biogeochemical processes within sediment is a high priority for aquatic and marine geochemistry (Boudreau, 2000). In fact, modeling is necessary not only to gain fundamental knowledge but also to enable fusion and interpretation of more detailed measurements due to advances in observational capabilities. Our goal is to use a mechanistic quantitative framework for investigating the coupled processes and to illustrate sensitivity of the reactive processes, if any, to sediment permeability. We hope to constrain in-situ nitrogen transformation rates that are not only difficult to measure in the field but have been challenging to computationally model as well. Our models are based on field- and laboratory-derived geometric, kinetic and hydraulic parameters.

2. Methods

2.1. Large-eddy simulation of turbulent-oscillatory flow over ripples

The space-filtered, transient, three-dimensional Navier–Stokes equations, typical in LES (see Pope, 2000 for details), are solved for turbulent flow over ripples by using a commercially available, unstructured, finite-volume computational fluid dynamics software, FLUENT (version 6.2.16). The subgrid-scale (SGS) stresses are modeled by the dynamic SGS kinetic energy model proposed by Kim and Menon (1999). A three-dimensional (3D) box-shaped computational domain is constructed using field-measured ripple topography as the bottom boundary and a flat top boundary. Three adjacent ripples were considered with a total horizontal or x-direction length of ~2 m. The depth of the water column domain is ~1 m (in the z-direction) and is discretized by 57 grid points with a smallest vertical mesh size of ~2 mm closest to the bed surface and with a vertical stretching factor of 1.055 (Fig. 1a). The span-wise (y direction) domain is 35 cm. Grid spacing in both x and y direction is 1 cm.

A no-slip boundary condition is applied at the ripple bottom boundary with a near-wall treatment based on the wall functions proposed by Werner and Wengle (1991). A shear-free boundary condition is used at the top boundary. The boundaries in the x–z-plane are periodic, while the boundaries in the y–z-plane are two time-dependent velocity inlets forced synchronously by measured time series of free stream (horizontal) velocities. The domain consists of three straight-crested ripples in line in the x-direction, which is long enough (as compared to the wave orbital diameter) to minimize the effect of the side boundaries (y–z-plane) on the evolution of turbulent flow over the ripple in the middle. The bounded central differencing scheme is used for spatial discretization while the temporal discretization follows the second-order implicit formulation with a time-step of 0.005 s. The pressure–velocity coupling adopts the fractional step method (FSM) under the non-iterative time advancement (NITA) option.

The field data used to drive the LES and for model-data comparison were measurements of seafloor ripples under wave-dominated conditions at the Martha's Vineyard Coastal Observatory (MVCO) site (Traykovski, 2007). The measurements consisted of

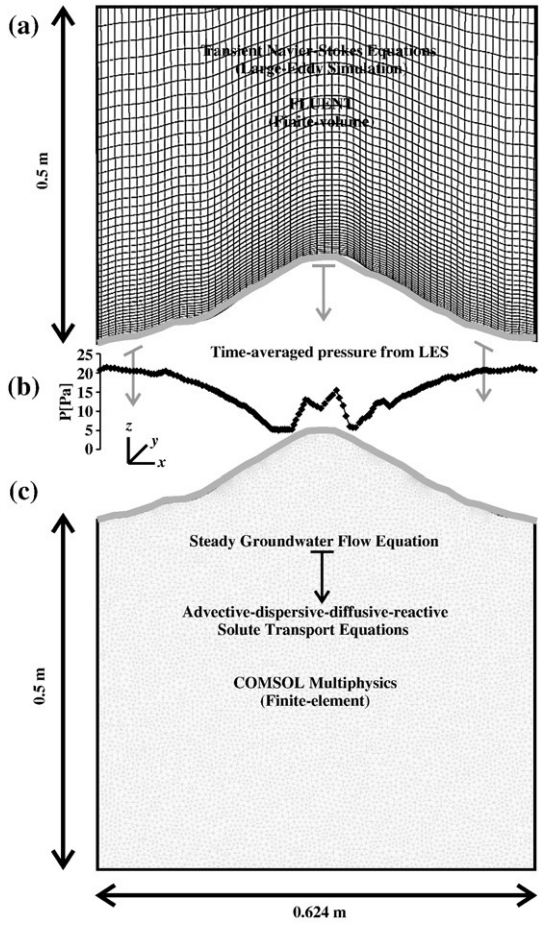

Fig. 1. Modeling scheme. a) Hexahedral grid for finite-volume Large-eddy simulation (LES) of oscillatory turbulent flow over a ripple surface (shown is middle of three ripples and bottom half of domain used for the LES). b) Time-averaged pressure profile along the sediment–water interface. c) Triangular mesh for finite-element simulation of pore water flow and reactive solute transport. The time-averaged pressure profile from the LES (inset) is imposed as boundary condition to the sediment flow and transport model.

backscatter imagery from rotary side-scan sonars, centimeter resolution bathymetric maps from a two-axis rotary pencil-beam sonar, and time series observations of free stream velocities that are used to force the LES. The measured waves were not purely sine or cosine waves but quite irregular, with wave periods mostly between 4–10 s and with velocity amplitudes of up to 1 m s^{-1}. Also measured were 30 cm profiles of vertical velocity sampled at 16 Hz with 0.8 cm resolution over a known location on the ripple topography, that can be compared to vertical velocity profiles obtained from the LES. A typical LES run was driven by a field-measured time series of free stream velocities of several hundreds of seconds in real time. The simulation was initialized by uniformly applying the free stream velocity as the streamwise velocity over the whole computational domain. Therefore, the first 50 s of simulated data was discarded due to initial spin-up.

2.2. Pore water flow through the ripple sediment

Flow through porous and permeable sediment is governed by the coupled groundwater flow equation and Darcy's Law:

$$\nabla \cdot \mathbf{q} = 0 \tag{1}$$

$$\mathbf{q} = -\frac{k_p}{\mu}\nabla P \tag{2}$$

where $\mathbf{q}$ is the specific discharge vector (i.e. Darcy flux) and k_p is intrinsic permeability, μ is fluid viscosity and P is pressure. The top boundary of the sediment, the SWI, is a Dirichlet boundary that takes on the time-averaged pressure from the LES simulations (Fig. 1b), thereby linking or sequentially coupling the two domains. The lateral and bottom boundaries are no-flow boundaries. The lateral boundaries are effectively flow divides when they coincide with the crest of the ripple, as is the case here, making a no-flow boundary suitable. The bottom no-flow boundary may strongly affect the flow field when it is too close to the top boundary. We conducted several simulations that show that the flow field near the SWI is hardly affected by this boundary at the location used for all simulations presented here (0.5 m below the trough).

2.3. Reactive transport modeling of the sediment

Reactive transport through the sediment is described by:

$$\frac{\partial C_i}{\partial t} + \nabla \cdot \left(-D_i^* \cdot \nabla C + \mathbf{v}C\right) = R_i \tag{3}$$

where C denotes the concentration for species i, D^* is the effective dispersion coefficient, $\mathbf{v}$ is pore velocity ($\mathbf{q}/\phi$, and ϕ is porosity=0.3), and R is the reaction rate (sink/source term). The effective dispersion coefficient is the sum of mechanical dispersion coefficient and the diffusion coefficient:

$$D^* = D_m + D \tag{4}$$

D_m, the mechanical dispersion tensor is defined as follows (de Marsily, 1986):

$$D_{m,ij} = \alpha_T U \delta_{ij} + (\alpha_L - \alpha_T) v_i v_j / V \tag{5}$$

where α_T and α_L are transverse and longitudinal dispersivities, V is the pore velocity magnitude, and δ_{ij} is the Kronecker delta function. α_L is set to 1 cm, equivalent to several grain diameters, that is typical for the scale of our simulations (e.g., de Marsily, 1986), and α_T is considered to be 1/10 of α_L. The diffusion coefficient is corrected for tortuosity following Boudreau (1996):

$$D = (1 - 2\ln\phi)^{-1} D^{mol} \tag{6}$$

where D^{mol} represents the molecular diffusion coefficient, that is calculated as a function of temperature and salinity using the relations given by Boudreau (1997).

The reaction rates R_i in Eq. (3) are calculated from the following reaction set:

$$\text{(aerobic respiration AR) } CH_2O + O_2 \rightarrow CO_2 + H_2O \tag{7}$$

$$\text{(denitrification DN) } CH_2O + 0.8NO_3^- + 0.8H^+ \rightarrow CO_2 + 0.4N_2 + 1.4H_2O \tag{8}$$

$$\text{(ammonification AM) } \{NH_3\}_{OM} + H^+ \rightarrow NH_4^+ \tag{9}$$

$$\text{(nitrification NI) } NH_4^+ + 2O_2 \rightarrow NO_3^- + H_2O + 2H^+. \tag{10}$$

The rates of aerobic respiration and denitrification were modelled using the classical cascade formulation for electron acceptors (Van Cappellen and Wang, 1996; Boudreau, 1997; Berg et al., 2003; Meysman et al., 2003) and are as follows:

$$R_{AR} = R_{min}\frac{[O_2]}{[O_2] + K_{O_2}^{sat}} \tag{11}$$

$$R_{DN} = R_{min}\frac{K_{O_2}}{[O_2] + K_{O_2}^{inh}}\frac{[NO_3^-]}{[NO_3^-] + K_{NO_3^-}^{sat}}. \tag{12}$$

Mineralization rates within sandy sediment have previously been observed to vary widely with depth (Jahnke et al., 2005; Cook et al., 2007). The volumetric remineralization rate $R_{\min}$ (expressed per unit volume of pore water) was varied as a function of sediment depth, taken from the SWI, according to the expression:

$$R_{\min} = R_{\min(0)} e^{\frac{-z_s^2}{\lambda^2}} \tag{13}$$

where z_s is the vertical distance from the SWI. $R_{\min(0)}$ in Eq. (13) was set to 340 μmol L^{-1}sed d^{-1} following (Cook et al., 2006), and λ was set to 0.1 m, giving a depth-integrated mineralization rate of 1133 μmol m^{-2} h^{-1} that falls in the middle to upper range of benthic respiration rates measured on shelf sediment (Reimers et al., 2004; Jahnke et al., 2005; Janssen et al., 2005). The half-saturation constants $K_{O_2}^{sat}$ in Eq. (11) and $K_{NO_3^-}^{sat}$ in Eq. (12) were set to 10 μM and 30 μM respectively, and the O_2 inhibition constant for denitrification $K_{O_2}^{inh}$ in Eq. (12) was also set to 2 μmol L^{-1}. Initial concentrations of solutes in the water column were as follows $[O_2]$=260 μM, $[NO_3^-]$=5 μM (base case, this was varied in some simulations), and $[NH_4^+]$=1 μM, that we regard as representative concentrations of nutrients for shelf bottom waters.

Organic carbon mineralization through other pathways like sulfate and Fe/Mn reduction were not modelled explicitly except in a few cases where sulphate reduction was included. However, the ammonium produced in these respiratory pathways was accounted for through the ammonification rate:

$$R_{AM} = \gamma_{NC} R_{\min}. \tag{14}$$

The ratio γ_{NC} of NH_4^+ produced to C mineralized was set to the value 1/6.6 assuming redfield C:N stoichiometry. Finally, nitrification was modelled using bimolecular kinetics:

$$R_{NI} = k_{NI}[O_2]\left[NH_4^+\right] \tag{15}$$

where k_{NI} is the nitrification constant, that was set to 12.5 μM^{-1} y^{-1} comparable to values of 5–29 μM^{-1} y^{-1} commonly used in the literature (e.g., Wang and Van Cappellen, 1996; Soetaert et al., 1996; Berg et al., 2003).

2.4. Initial and boundary conditions

Eqs. (1) and (2) were solved with the SWI prescribed the time-averaged pressure distribution along the interface determined by the LES for turbulent-oscillatory flow over ripples (Fig. 1b). The pressure was averaged over a period of ~150 s, representing several wave periods that varied around 4–10 s, after a spin-up cycle of 50 s, with output every 0.1 s. The vertical boundaries of the sediment are spatially periodic boundaries while the bottom boundary is a no-flow boundary.

Prior to conducting reactive transport simulations, we first conducted simulations with a non-reactive solute (dye) and then for a single-reacting solute, O_2, whose consumption is described by Eq. (11). Afterwards, we considered two scenarios for coupled multi-species reactive transport of O_2, NO_3^-, and NH_4^+ by imposing different initial conditions in the sediment (see Discussion for a justification of this approach). Sensitivity analysis with varying permeability is conducted for these two settings. Additional simulations were run to investigate the effects of SO_4^{2-} reduction and dependency on mineralization profiles (λ).

The first scenario corresponds to well-flushed sediment conditions reflecting what might be expected after a storm resuspension event; this is referred to as the resuspension case. For this simulation, the initial solute concentrations in the 15 cm of sediment were set to the same as the water column and then dropping off to 0 abruptly via a steep exponential function.

Initial conditions reflecting a more settled period are based on the observations by Jahnke et al. (2005) collected from the South Atlantic Bight; this is referred to as SAB conditions. For this simulation, the initial concentrations of O_2 and NO_3^- in the sediment were set to 0, and NH_4^+ was set to 30 μM uniformly throughout the sediment. Additional simulations were also run to investigate the effect of permeability and water column NO_3^- concentration on denitrification.

The top boundary of the sediment is divided into two types of boundaries. Where water is flowing into the sediment, a constant concentration corresponding to the concentration of species i in the water column, defined above, is prescribed (Table 1). Areas where pore water is flowing out of the sediment and back into the water column are considered convective or zero-normal gradient boundaries. The vertical boundaries are again considered as spatially periodic boundaries. The bottom is a zero flux boundary. Unless otherwise stated, the parameters in the models follow those in Table 1.

Both flow and transport processes in the sediment are simulated using the generic finite-element software COMSOL Multiphysics (COMSOL AB, 2006). Quadratic triangular elements are used in both pore water flow and transport simulations. The domain typically contains more than 16,000 elements, with finer mesh size near the SWI (Fig. 1c).

3. Results

3.1. Oscillatory turbulent flow field and pressure along the sediment–water interface

The LES results (Fig. 2) and field observations agree well in terms of both spectral analysis and vertical velocity profiles along a vertical line above the ripple crest. This analysis of the LES performance is discussed elsewhere and is forthcoming (Jiang and Traykovski, 2006; manuscript in preparation). The y-direction-averaged and time-averaged total pressure profile along the ripple surface (Fig. 1b) is similar to previous studies where the high pressures are found near the ripple troughs and low pressures are present where vortices are shed near the crest. However, two local pressure highs are present along the crest. This is possibly due to local topography in the crest (Fig. 1a) that leads to pronounced and locally constrained vortex shedding similar to those observed by Ourmieres and Chaplin (2004). Note that the crest is asymmetric with the highest point towards the right. These small-scale topographic variations are not present in studies that consider idealized sinusoidal sand ripples (e.g., Shum and Sundby, 1996). Moreover, the flow simulation was forced by field

Table 1
A summary of the parameters used to set up the model used in the model simulation of sediment biogeochemical processes in permeable sediment

Symbol	Unit	Value	Description
$K_{O_2}^{sat}$	μM	10	Half saturation constant for O_2 limitation of oxic remineralization
$K_{NO_3^-}^{sat}$	μM	30	Half saturation constant for NO_3^- limitation of denitrification
$K_{O_2}^{inh}$	μM	2	Half saturation constant for O_2 inhibition of denitrification
k_{NI}	μM^{-1} y^{-1}	12.5	Nitrification rate
$R_{\min(0)}$	μmol L^{-1} sed d^{-1}	340	Maximum rate of aerobic organic matter oxidation and denitrification (as C equivalents)
$\gamma_{N:C}$	–	1/6.6	Net production of NH_4^+ in relation to C mineralized
ϕ	–	0.3	Sediment porosity
λ	m	0.1	Depth extinction parameter
α_L	m	0.01	Longitudinal dispersivity
$[NO_3^-]$	μM	5	Concentration in the water column and inlet boundaries
$[NH_4^+]$	μM	1	Concentration in the water column and inlet boundaries
$[O_2]$	μM	260	Concentration in the water column and inlet boundaries

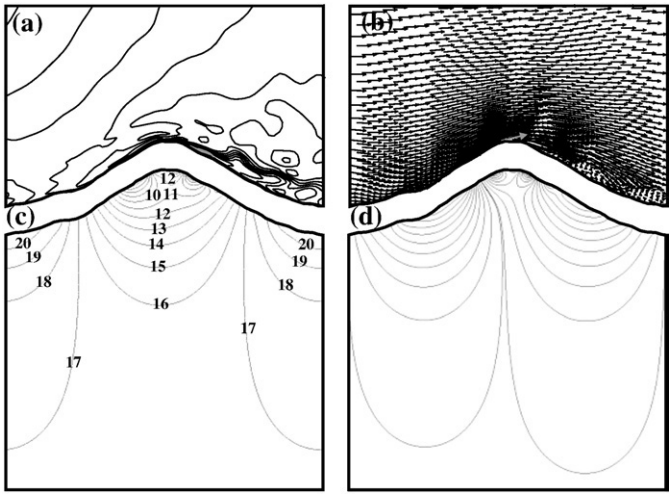

Fig. 2. Simulated flow fields. a) Time-snapshot of pressure from LES simulation of turbulent-oscillatory flow; thick gray line near the crest corresponds to $P=0$ Pa, contour interval = 16 Pa. b) LES time-snapshot of velocity; largest vector (gray arrow) corresponds to $U=0.862$ m/s. c) Pore water flow pressure field (P in Pa). d) Pore water flow streamlines.

observations with highly irregular wave periods, unlike in previous laboratory experiments or computational and analytical analyses where the wave-period is idealized. The averaged pressure profile defines the Dirichlet boundary condition along the sediment–water interface for the pore water flow model.

3.2. Flow field in the sediment and transport of a conservative solute

The flow field in the sediment is similar to those observed in laboratory experiments where there is flow toward a low pressure area in the crests (Fig. 2). However, since the LES simulations also generated pressure highs at the crests, this also results in local flow and flushing from this area (Fig. 2). Transport simulation for a conservative solute, i.e., $R=0$ in Eq. (3), results in a distribution that is very similar to those of dye being washed out from sediment in laboratory experiments (Fig. 3). The solute initially starts as filling the entire sediment and later flushed by "clear" bottom water infiltrating from pressure highs along the SWI.

3.3. Reactive transport simulations and sensitivity of reaction rates to permeability

The results presented here are based on flow and transport simulations simultaneously considering three different species (O_2, NO_3^-, and NH_4^+, plus SO_4^{2-} and HS^- in a few cases). Fig. 4 illustrates the distribution of oxygen after three days for four different permeability cases with a starting condition representing storm resuspension. Fig. 4a ignores the effects of advection, i.e., $\mathbf{v}=(0, 0, 0)$, and transport is by diffusion only. This situation may be due to very quiescent conditions in the water column or very low permeability values. The remnant patch of O_2 is later on consumed completely resulting in completely anoxic conditions in the sediment. Imposing a permeability value typical of fine sand (Fig. 4b) results in a very different O_2 distribution. The initially available reservoir of O_2 is flushed towards the crest leaving only a small stretched plume that is also consumed later on. However, oxygenated bottom water infiltrates into the sediment resulting in pockets of oxygen-rich areas under the troughs. This oxygen-rich zone grows with increasing magnitude of advection driven by increasing permeability (Fig. 4c and d). Note that we use the same boundary conditions for the flow field in all simulations, only the permeability is changed. The spatial patterns of O_2 distribution agree well with both flume and in-situ measurements to date (Fig. 4, Huettel et al., 1998; Precht et al., 2004), and this work is the first to simulate the in-situ distribution of solutes based on measured in-situ ripple geometries and bottom currents.

Results of multi-species and coupled reactive flow and transport simulations of the sediment show a complex pattern of temporal evolution reflecting the competition between transport and production/consumption rates (Fig. 5). Results for simulations with the same permeability (0.5×10^{-10} m^2) but with the two different initial conditions are presented up to 2.5 d every 12 hour period. The patterns observed contrast sharply with the classical diffusive solute distribution patterns observed in fine sediment that generally show a steady increase or decrease in solute concentrations with depth in the sediment. Interestingly, results show that one would expect to find broad zones of high nitrate concentration below the oxic zone of the sediment. Reconciling this expected nitrate distribution with observations is difficult because most sampling methods (e.g., coring) will laterally integrate the nitrate concentrations. Furthermore, the likely flushing conditions of permeable sediment studied to date are hard to predict because important parameters such as ripple geometry, permeability and bottom currents are seldom simultaneously reported, if at all. Nevertheless, our simulations are consistent with observed nitrate concentrations in excess of 10 μM, in the anoxic zone of permeable sediment (Lohse et al., 1996a).

For the resuspended initial condition there were, in some instances, strong temporal changes in the evolution of solute distributions (Fig. 5) as well as in nitrification and denitrification rates (Fig. 6) that were dependent upon the sediment permeability. In sediment with low permeability and low flushing rate, the rate of O_2 transport into the sediment was relatively low and as a result, the pool of O_2 initially present was consumed, with a cascading effect on the N cycle. In the presence of O_2, nitrification rates were initially high, and then declined as O_2 was consumed. Once the O_2 had been consumed, the rate of denitrification increased to ~80 μmol N m^{-2} h^{-1} as the pool of NO_3^- in the formerly oxic zone of the sediment was denitrified. Denitrification rates dropped rapidly again once this NO_3^- pool was consumed. For the most permeable sediment and highest flushing rate, there was little change in the rates over time (Fig. 6). We ascribe this observation to the fact that high flushing rates will lead to high rates of O_2 transport into the sediment, giving rise to an extensive oxic zone; a situation similar to the starting condition. For the SAB initial condition, the rates of nitrification, denitrification and sediment O_2 consumption increased steadily and generally approached rates close to steady state within 12 h of the simulations commencing. After 72 h, the rates of these processes were virtually the same for the two starting conditions under all permeability scenarios.

Quasi-steady state nitrification, denitrification and sediment O_2 consumption rates all showed significant variation with sediment permeability (Fig. 7). Nitrification rates initially dropped slightly (~25%) in the transition from a diffusive to an advective transport regime, followed by a steady increase, up to permeabilities of 0.7×10^{-10} m^2, before reaching a plateau at higher permeabilities. Denitrification rates

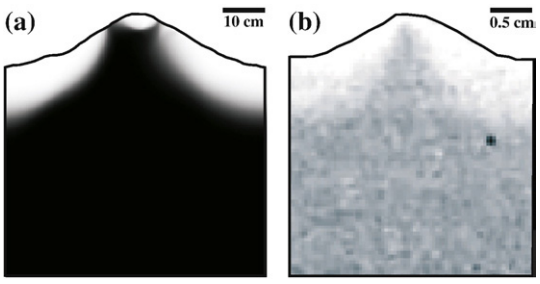

Fig. 3. Comparison of simulated and experimental washout patterns. a) Conservative solute distribution for washout simulation after 1 d; permeability = 0.15×10^{-10} m^2. b) Observed dye washout in a wave tank; permeability = 0.29×10^{-10} m^2 (modified Huettel et al., 2003).

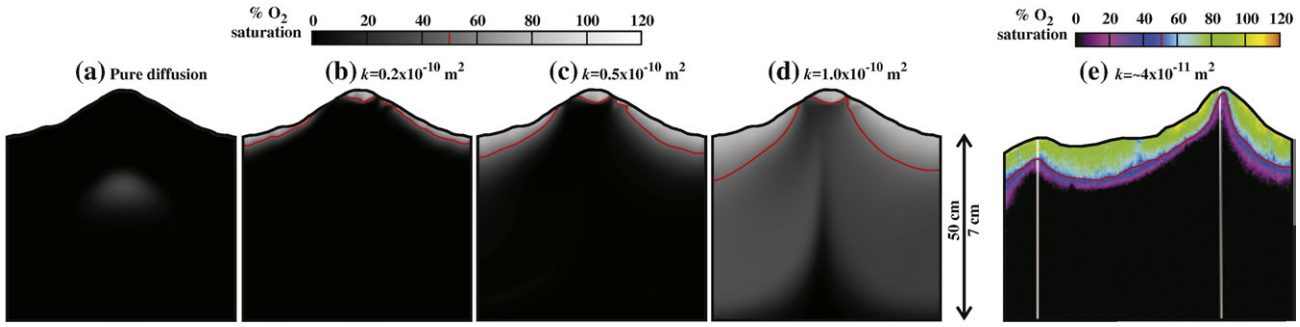

Fig. 4. Comparison of simulated and experimental oxygen distribution. a) Pure diffusion case (no advection in sediment). b–d) Simulations for sediment with increasing permeability. e) In-situ oxygen distribution observed with planar optode (modified after Cook et al., 2007).

increased by a factor of ~3 as the sediment permeability increased from 'diffusive' up to a permeability of 0.5×10^{-10} m^2. Above this threshold, denitrification rates dropped rapidly by a factor of ~4 with a further doubling of the sediment permeability. The impact of sediment permeability on denitrification rates is graphically illustrated in Fig. 8, where it can be seen that under diffusive conditions and low permeability, denitrification is restricted to a thin band below the SWI. At intermediate permeabilities, the denitrification zone is consolidated to one 'hotspot' below the ripple crest. At the highest permeabilities, this hotspot disappears owing to the completely oxic nature of the sediment.

3.4. Effect of sulfate reduction and mineralization depth

We ran a subset of models including sulfate reduction at sediment permeabilities of 0 (diffusive), 0.05×10^{-10} and 1×10^{-10} m^2 (Supplemental Fig. 1). The net result was that adding in sulfate reduction led to virtually no change in the process rates including O_2 consumption. Under diffusive conditions, the run time of 3 d was insufficient to reach any thing near a steady state, and hence sulfide was building up faster than it was being oxidized (and consuming O_2). Under advective conditions when we would expect a situation close to steady state to develop within 3 d, the lack of change is due to the release of reduced sulfide from focused outflow points near the ripple crests. Ignoring sulfate reduction and sulfide reoxidation in the model scheme for permeable sediment is therefore justified.

Another subset of simulations was run with different depth attenuation coefficients (λ) effectively reducing the depth dependency of denitrification. The integrated mineralization rates were held constant by corresponding adjustments in the mineralization rate ($R_{\min(0)}$). Denitrification rates are about 20% lower with depth attenuation coefficients of 0.2–0.4 m, compared to our previously used value of 0.1 m (Supplemental Fig. 2). Thus, the model does show some depth sensitivity to total denitrification, however it is relatively small. Oxygen distributions are similarly slightly sensitive to λ (Supplemental Fig. 3).

4. Discussion

4.1. Simulation approach

Sands are highly dynamic and non-deterministic environments in comparison to cohesive muds and this is one of the obstacles to process-based simulation of these environments. In the high energy environments in which sand deposits form, resuspension events will commonly occur leading to solute concentrations within the surface sediment initially reflecting those within the water column. After this 'resetting', there will be a rapid transformation of solute distributions and concentrations within the sediment reflecting the transport regime and solute production/consumption rates. After a long period of calm and, hence, lower transport rates within the sediment, there will be a relative build up of reduced solutes within the sediment. As such, basing estimates of process rates on steady state solutions of models (as is standard practice for reactive transport models in cohesive sediment) may not be realistic in permeable sediment. The starting point for model simulations is arbitrary and, given the limited availability of data, we have chosen to use nutrient concentrations measured within South Atlantic Bight sediment (Jahnke et al., 2005), as well as a hypothetical flushing event based on observations made in the field (Cook et al., 2007). Even with these very different starting conditions, the process rates converged within 24 to 72 h, and we are therefore confident that our results are not biased by our arbitrarily chosen initial solute distributions.

4.2. Reaction rates and the role of advective pore water exchange

To date, accurate estimates of nitrification and denitrification in permeable sediment remain poorly constrained. Measurements of denitrification in sandy sediment have virtually all been conducted in small diameter core incubations, e.g., Lohse et al. (1996b) and Vance-Harris and Ingall (2005), that neglect advective pore water transport. Numerical simulations have shown that advective pore water flow fields within benthic chambers have a significant impact on nitrification and denitrification rates (Cook et al., 2006), highlighting the importance of advective pore water transport in controlling nitrification and denitrification rates. The results of the present study further underscore the importance of advective pore water transport in controlling nitrification and denitrification rates under natural conditions and provide the first estimates of these processes in sediment affected by advective pore water transport.

The observed enhancement of nitrification and denitrification with advective flushing is in agreement with the previous study of Cook et al. (2006). In contrast to this previous study though, we found denitrification decreased above a permeability of 0.5×10^{-10} m^2, and dropped below rates estimated for the diffusive scenario above a permeability of 0.8×10^{-10} m^2. We ascribe this difference to marked differences in the geometry of the denitrification zones modelled by Cook et al. (2006) for a chamber setting. In our current study, it can be seen that the geometry of the denitrification zone was highly irregular, changing from an arc shape at low permeabilities to an amorphous hotspot below the ripple crest at intermediate to higher permeabilities (Fig. 8). This contrasts with the geometry of the denitrification zone simulated by Cook et al. (2006), a regular broad arc that increased in size over the flushing rates simulated. For comparison, we have shown the model results of Cook et al. (2006) run with the same parameter values to the current simulations (Fig. 7). The main difference between the two models is the geometry of the flow fields. This is enough to drive a marked deviation in the process rates, with nitrification and denitrification being higher at intermediate sediment flushing rates in the current study. At higher flushing

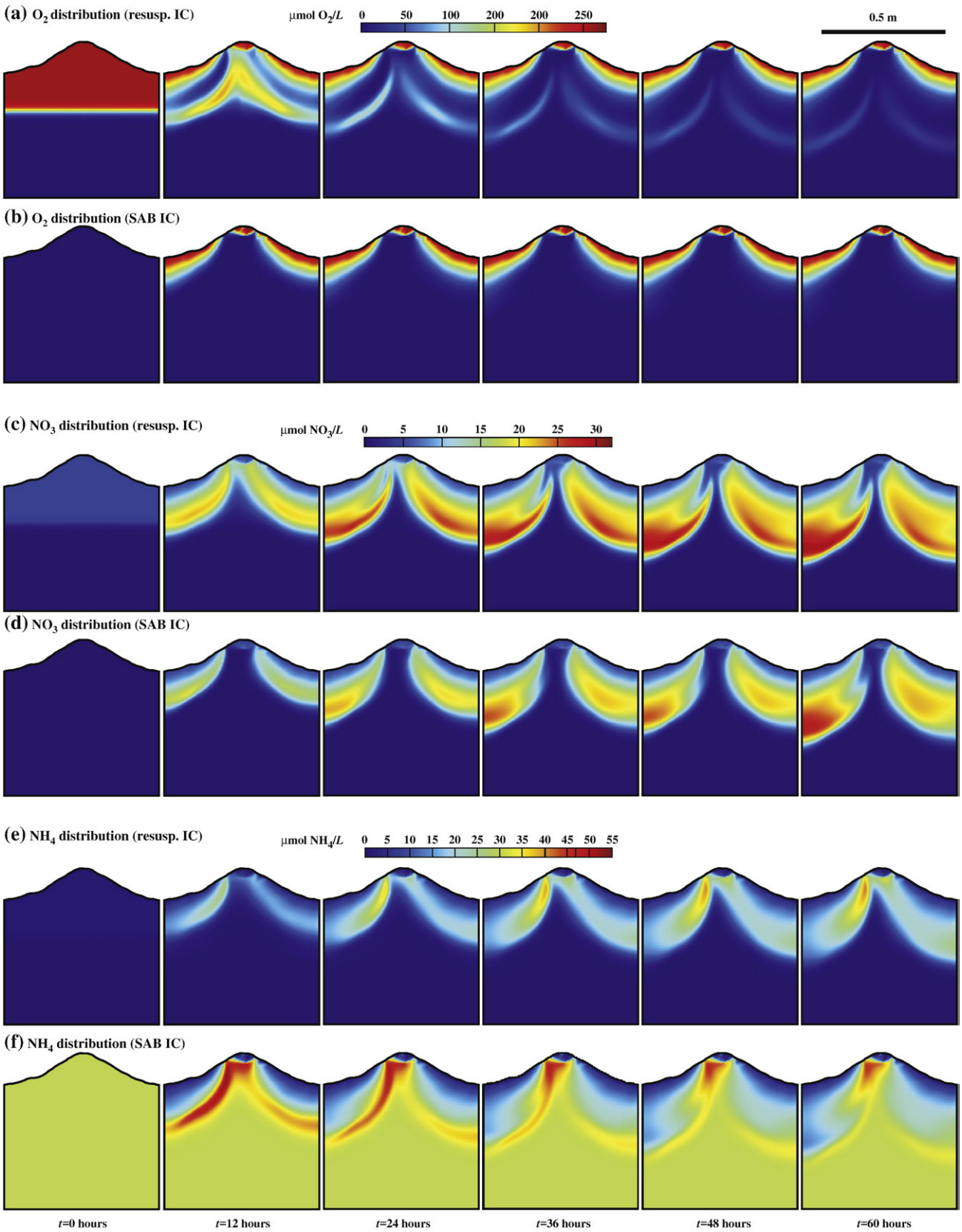

Fig. 5. Simulated results of coupled biogeochemical transport and transformation at 12 hour intervals. a, b) Oxygen distribution for initial conditions representing a resuspension event and conditions at the South Atlantic Bight (Jahnke et al., 2005), c, d) Nitrate distribution and e, f) Ammonium distribution for the two initial conditions. Permeability for all simulations is 0.5×10^{-10} m^2.

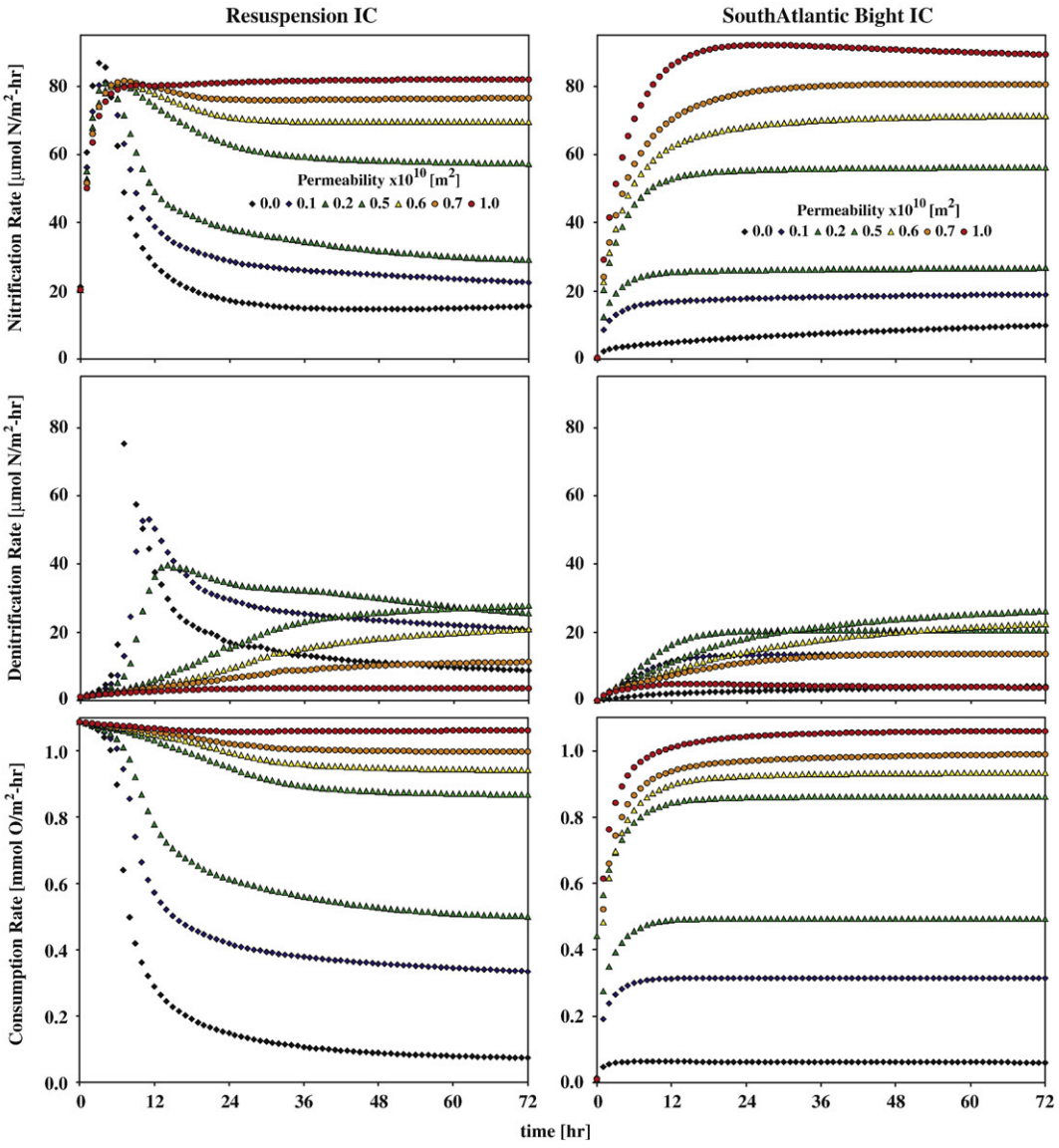

Fig. 6. Integrated reaction rates (normalized per area of sediment–water interface) for different sediment permeability and initial conditions. Those on the left column (a, c, e) are described by a well-mixed initial condition typical after a resuspension event, those on the right (b, d, f) start from initial conditions following Jahnke et al.'s (2005) observations from the South Atlantic Bight (SAB).

rates, there was no drop in the denitrification rates simulated within chambers, as observed here. From a mechanistic viewpoint, these observed differences can be explained as follows. At intermediate flushing rates, the flow path length and sediment O_2 consumption rate in the current simulation allowed the formation of an anoxic site below the ripple crest (Fig. 7). Relatively high rates of nitrate transport into this zone allowed high denitrification rates to take place. At increasing flushing rates, O_2 is flushed into the formerly anoxic region of the sediment at a rate faster than it can be consumed. Under this scenario, denitrification becomes inhibited by the presence of O_2 within the sediment. In the case of the chamber simulation, the flow field geometry exhibited poorly flushed regions within the sediment and anoxia developed within the sediment at all flushing rates. As such, no decrease in denitrification occurs at high flushing rates. The existence of poorly flushed regions in the sediment, while it enhances the availability of anoxic locations for denitrification to occur, results in poor transport of nitrate into this zone, so maximum denitrification rates are not as high as for the ripple simulation. Thus, the character of the flow field can be just as critical as the kinetic parameters and the sediment permeability (flushing rates) in determining biogeochemical process rates. Sediment denitrification rates will be at their optimum at intermediate sediment permeabilities and flushing rates. In cohesive sediment, similar optimal rates of denitrification occur that are controlled by sediment mineralization rates (Soetaert et al., 2000).

The sediment permeability plays an important role in determining the response of nitrification and denitrification rates following a resuspension event. At the lowest sediment permeabilities ($<0.2\times10^{-10}$ m^2), there was a transient spike in nitrification and denitrification rates. In such sediment, frequent resuspension events may substantially increase total sediment denitrification rates, above what would otherwise take place under more settled conditions.

We note that these simulations suggest that a relatively small fraction of total N mineralized is lost through denitrification. A direct comparison of the denitrification rates estimated here with those measured in cohesive sediment is difficult because it will be confounded by factors such as sediment respiration rates, the presence of photoautotrophic biomass, and water column NO_3^- concentrations. Based on a simulation analysis of sediment denitrification rates under a range of conditions by Soetaert et al. (2000), one would expect ~20–30% of the N mineralized in the sediment to be

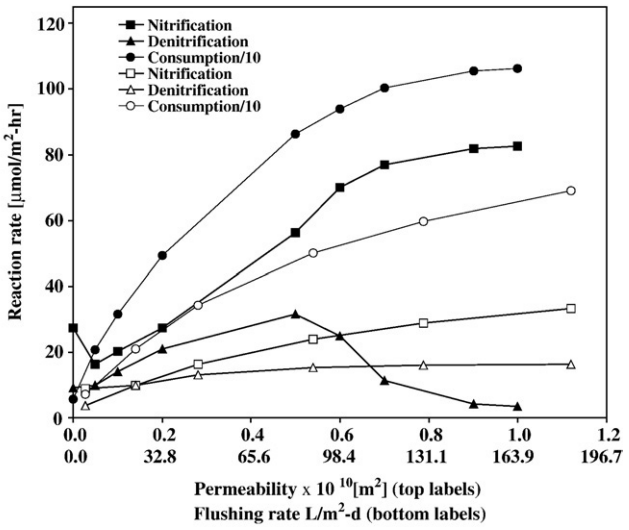

Fig. 7. Quasi-steady state reaction rates (R_i at 15 d) per unit surface area of sediment for different permeabilities and flushing rate scenarios and initial conditions modeled after a resuspension event (solid symbols). Also shown for comparison are the results from the model of Cook et al. (2006) using the same parameter values (open symbols). Note that the oxygen consumption rate is divided by 10 to fit in the same axis. The reaction rates for the South Atlantic Bight initial conditions are practically the same.

released as N_2 gas at mineralization rates of ~1000 μmol m^{-2} h^{-1}. In the present study, the maximum loss of N as N_2 gas was ~15% of the total N mineralization, and in general, it was much lower than this, particularly under diffusive and highly permeable conditions. This suggests that sands remove a relatively small amount of nitrogen via denitrification in comparison to cohesive sediment. One contributing factor to the lower rates of denitrification in sandy sediment is their relatively low porosity. Running the current model at a higher porosity of 0.9 more typical of fine muddy sediment results in a doubling of the denitrification rate under the diffusive scenario (data not shown).

The water column nitrate concentration influences denitrification in cohesive sediment, with denitrification rate generally increasing linearly with NO_3^- concentration. The water column nitrate concentration also affects denitrification in permeable sediment but the influence is not exclusively linear due to additional influence of sediment permeability/flushing rate (Fig. 9). At low to intermediate permeabilities ($0.1–0.6\times10^{-10}$ m^2, 16–98 L/m^2 d flushing rates), nitrate concentration exerts a strong and almost linear influence over denitrification at concentrations of up to 50 μM. At higher flushing rates, however, denitrification is much less influenced by the NO_3^- concentration in the water column. Under such conditions, it is not the rate of transport of NO_3^- to the denitrification zone that limits denitrification, rather, it is controlled by the extent of the anoxic zones within the sediment where denitrification can take place. This observation critically underscores the importance of sediment permeability in regulating the sediment denitrification rate, and suggests that in shelf sediment with permeabilities above a critical threshold of $\sim0.7\times10^{-10}$ m^2, there may be negligible rates of denitrification.

Our model results also need to be reconciled against actual measurements of denitrification in permeable shelf sediment (these are very rare). We note that obtaining realistic measurements of denitrification in permeable sediment is difficult and currently used measurement techniques will each suffer from their own specific set of disadvantages. The emplacement and stirring mechanism of chambers may lead to a non-steady state release of N_2 from the porewaters leading to erroneously high flux estimates (Cook et al., 2006). The use of small diameter intact sediment cores will result in essentially diffusive incubation conditions and, hence, underestimate denitrification (Cook et al., 2006). Flow through reactors such as those used by Rao et al. (2007) will ensure steady state measurements, however, the rate of denitrification may be very different to that occurring in-situ owing to changes in the size and shape of the porewater flow field.

Our modeled rates are generally much lower (<50%) than the average value of ~70 μmol m^{-2} h^{-1} obtained from chambers in permeable sands (Laursen and Seitzinger, 2002), at comparable water column NO_3^- concentrations of <5 μM. This is consistent with the limitations of experimental methods outlined above. Conversely, our modeled rates were generally higher than the rates reported for small intact core incubations of sand (~1–13 μmol m^{-2} h^{-1}) (Lohse et al., 1996a; Vance-Harris and Ingall, 2005), and were in good agreement with the range of values measured using flow through column reactors (10–60 μmol m^{-2} h^{-1}, see Rao et al., 2007). Thus, our model results generally fell in the middle of the range of denitrification rates reported for sands within the literature. Within this context, we note that flow through column reactors are a relatively simple and reliable means of obtaining a first-order estimate of denitrification in permeable sediment. The further advantage of this approach is that the data from these experiments may be further used to refine model simulations.

Shelf sediment is thought to account for about a third to half of global benthic denitrification that was estimated to be 230–285 Tg N per year by Middelburg et al. (1996). The estimates of benthic denitrification by Middelburg et al. (1996) were based on a 1D steady state diagenetic model, that represents low-permeability sediment well, but is of uncertain value for estimating denitrification rates in permeable sediment. A simple direct comparison of the rates of

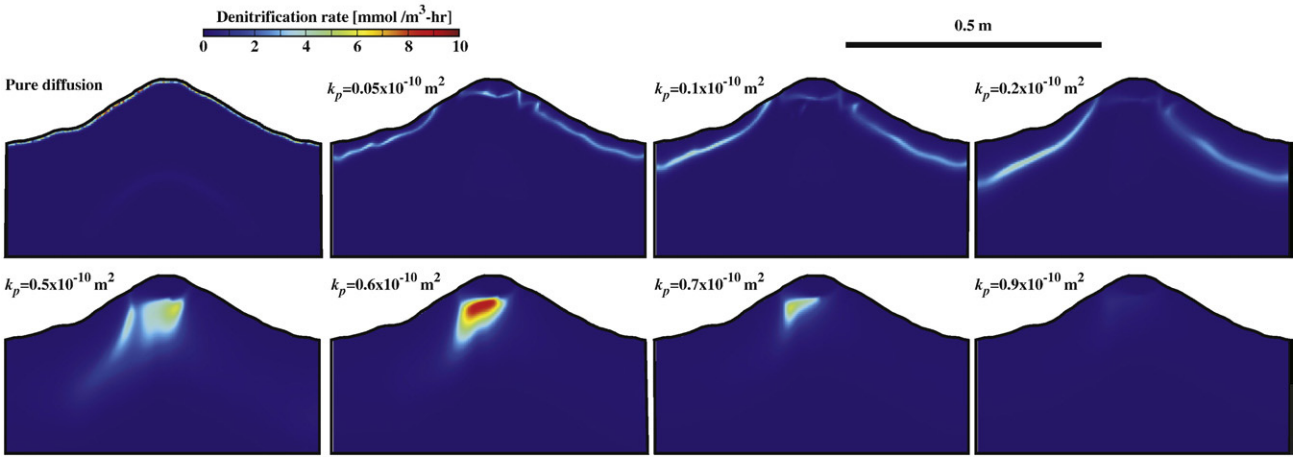

Fig. 8. Quasi-steady-state distribution of denitrification rates 15 d after resuspension for different permeability (k_p) sediments.

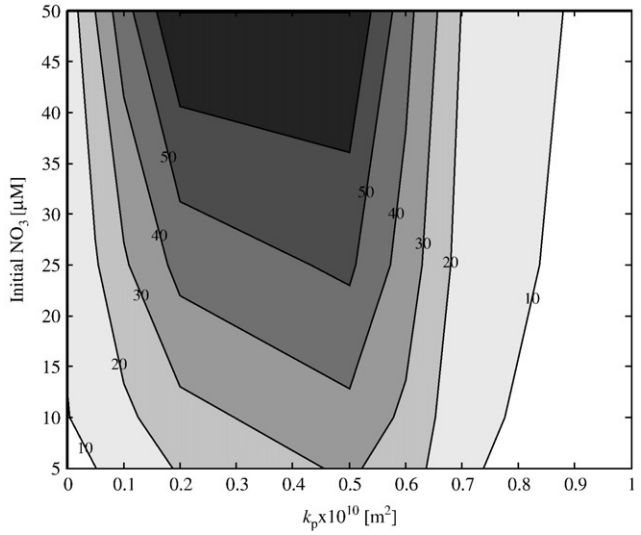

Fig. 9. Quasi-steady-state denitrification rates 15 d after resuspension for different permeability (k_p) sediments and water column/initial NO_3^- concentrations. Contour interval is 10 μmol m^{-2} h^{-1}.

denitrification expected in shelf sediment from that study compared to ours can be undertaken using the empirical meta model presented in Middelburg et al. (1996). At a carbon mineralization of 1133 μmol m^{-2} h^{-1}, with bottom water NO_3^- and O_2 concentrations of 5 and 260 μM respectively and at a depth of 100 m, the model of Middelburg et al. (1996) predicts a denitrification rate of 67 μmol m^{-2} h^{-1}. The highest rate of denitrification predicted by our model with the same sediment carbon mineralization and bottom water O_2 and NO_3^- concentrations was ~30 μmol m^{-2} h^{-1}, and much less than this at extremely low or high permeability (<10 μmol m^{-2} h^{-1}). Given that permeable sediment comprise ~70% of the shelf area, our model suggests that the study of Middelburg et al. (1996) may have over estimated denitrification rates on the shelf by a factor of 2–7 depending on the exact permeability and sediment flushing rates. Note that we fixed porosity in our simulations. Porosity affects solute flushing rates since the pore velocity is the Darcy velocity scaled by the porosity. This should be a topic of future modeling studies. Given, the critical role of sediment porosity and permeability, topography and bottom currents in controlling denitrification rates, we suggest that an improved knowledge of these factors is vital for obtaining better estimates of denitrification taking place on shelf sediment.

The finding that denitrification rates on shelf sediments may be lower than previously estimated is significant, because it has been suggested that there is an imbalance in the global N budget, with denitrification exceeding known inputs by 188–234 Tg N yr^{-1} (Codispoti, 2007). A large proportion of this imbalance comes from high benthic denitrification rates which Codispoti (2007) estimates to be in excess of 300 Tg N yr^{-1}, partly on the assumption that denitrification rates in sand are high. It is beyond the scope of this study to simulate denitrification rates over the entire shelf. However, some simple comparisons with the results of Middelburg et al. (1996) allow us to make some estimates of the implications of our findings for the global nitrogen budget. Middelburg et al. suggest that the global denitrification rate is in the range of 230–285 Tg N yr^{-1}, with ~100 Tg yr^{-1} of that taking place on the shelf. Given that 70% of the shelf sediments are sand and our model simulates rates 2–7 times lower than the model of Middelburg et al. (1996), then we estimate a shelf denitrification rate of 40–65 Tg yr^{-1}, giving a total oceanic denitrification rate of 170–250 Tg yr^{-1}. This estimate of denitrification is in reasonable agreement with the balanced budget of Gruber (2004), who estimated a global denitrification rate of 180±50 Tg N yr^{-1}. Our findings, therefore, suggest that estimates of global benthic denitrification rates in excess of 300 Tg yr^{-1} by Codispoti (2007) are likely to be an over estimate by ~50–130 Tg N yr^{-1} which accounts for ~20–70% of the N missing in his budget.

5. Conclusion

This paper further underscores the relative complexity of the biogeochemical function of permeable rippled sediment. For a given set of kinetic models and parameters, there may be a wide range of biogeochemical process rate outcomes depending on sediment hydraulic properties, bottom water flow and ripple topography. Observation and quantification of biogeochemical processes in permeable sediment is technically challenging, and we illustrate that advancing our fundamental understanding of this ubiquitous environment is made possible by linking high-fidelity hydrodynamic and reactive transport distributed models. This approach needs to be extended to a variety of ripple geometries, sedimentary conditions, and biogeochemical kinetics. Simulating multiple scenarios using our computationally-intensive approach will eventually lead to predictive models that may be used to estimate local or even shelf-scale storage and flux of important biogeochemical constituents.

Acknowledgments

This research was made possible through software and hardware support from the University of Texas at Austin Jackson School of Geosciences. Filip Meysman and Oleksiy Galaktionov helped formulate the kinetics used in our models. Houshuo Jiang and Peter Traykovski were supported by the Coastal Ocean Institute at the Woods Hole Oceanographic Institution and Office of Naval Research Grant N00014-06-10329. We thank Jack Middelburg and two anonymous reviewers, whose thoughtful and thorough review improved our manuscript.

Appendix A. Supplementary data

Supplementary data associated with this article can be found, in the online version, at doi:10.1016/j.epsl.2008.08.016.

References

Barr, B.C., Slinn, D.N., Pierro, T., Winters, K.B., 2004. Numerical simulation of turbulent, oscillatory flow over sand ripples. J. Geophys. Res. 109 (C9) Art. No. C09009.
Berg, P., Rysgaard, S., Thamdrup, B., 2003. Dynamic modeling of early diagenesis and nutrient cycling. A case study in an Arctic marine sediment. Am. J. Sci. 303, 905–955.
Boudreau, B.P., 1996. The diffusive tortuosity of fine-grained unlithified sediment. Geochim. Cosmochim. Acta 60, 3139–3142.
Boudreau, B.P., 1997. Diagenetic Models and Their Implementation: Modeling Transport Reactions in Aquatic Sediment. Heidelberg Germany, Springer.
Boudreau, B.P., 2000. The mathematics of early diagenesis: from worms to waves. Rev. Geophys. 38 (3), 389–416.
Boudreau, B.P., Huettel, M., Forster, S., Jahnke, R.A., McLachlan, A., Middelburg, J.J., Nielsen, P., Sansone, F., Taghon, G., Van Raaphorst, W., Webster, I., Weslawski, J.M., Wiberg, P., Sundby, P., 2001. Permeable marine sediment: overturning an old paradigm. EOS Trans. Am. Geophys. Union 82, 133–136.
Burnett, W.C., Bokuniewicz, H., Huettel, M., Moore, W.S., Taniguchi, M., 2003. Groundwater and pore water inputs to the coastal zone. Biogeochemistry 66, 3–33.
Cardenas, M.B., Wilson, J.L., 2007a. Hydrodynamics of coupled flow above and below a sediment–water interface with triangular bed forms: underflow case. Adv. Water Res. 30 (3). doi:10.1016/j.advwatres.2006.06.009, 01-313.
Cardenas, M.B., Wilson, J.L., 2007b. Dunes, turbulent eddies, and interfacial exchange with permeable sediment. Water Resour. Res. 43, W08412. doi:10.1029/2006WR005787.
Chang, Y.S., Scotti, A., 2003. Entrainment and suspension of sediment into a turbulent flow over ripples. J. Turbul. 4 Art. No. 019.
Chang, Y.S., Scotti, A., 2004. Modeling unsteady turbulent flows over ripples: Reynolds-averaged Navier–Stokes equations (RANS) versus large-eddy simulation (LES). J. Geophys. Res. 109 (C9) Art. No. C09012.
Codispoti, L.A., 2007. An oceanic fixed nitrogen sink exceeding 400 Tg Na-1 vs the concept of homeostasis in the fixed-nitrogen inventory. Biogeosciences 4, 233–253.
COMSOL AB, 2006. COMSOL Multiphysics User's Guide. Palo Alto California, COMSOL AB.
Cook, P.L.M., Wenzhöfer, F., Rysgaard, S., Galaktionov, O.S., Meysman, F.J.R., Eyre, B.D., Cornwell, J.C., Huettel, M., Glud, R.N., 2006. Quantification of denitrification in permeable sediment: insights from a two dimensional simulation analysis and experimental data. Limnol. Oceanogr. Methods 4, 294–307.

Cook, P.L.M., Wenzhöfer, F., Glud, R.N., Janssen, F., Huettel, M., 2007. Benthic exchange and mineralisation in two subtidal sandy sediment: effect of flow. Limnol. Oceanogr. 52, 1943–1963.
de Marsily, G., 1986. Quantitative Hydrogeology: Groundwater Hydrology for Engineers. Academic Press, Orlando Florida.
Gruber, N., 2004. The dynamics of the marine nitrogen cycle and its influence on atmospheric CO_2. In: Follows, M., Oguz, T. (Eds.), The Ocean Carbon Cycle and Climate. Kluwer Academic, Dordrecht, pp. 97–148.
Huettel, M., Gust, G., 1992. Impact of bioroughness on interfacial solute exchange in permeable sediment. Mar. Ecol. Prog. Ser. 89, 253–267.
Huettel, M., Ziebis, W., Forster, S., Luther III, G.W., 1998. Advective transport affecting metal and nutrient distributions and interfacial fluxes in permeable sediment. Geochim. Cosmochim. Acta 62, 613–631.
Huettel, M., Røy, H., Precht, E., Ehrenhauss, S., 2003. Hydrodynamical impact on biogeochemical processes in aquatic sediment. Hydrobiologia 494, 231–236.
Jahnke, R.A., Richards, M., Nelson, J., Robertson, C., Rao, A., Jahnke, D.B., 2005. Organic matter mineralization and pore water exchange rates in permeable South Atlantic Bight continental shelf sediment. Cont. Shelf Res. 25, 1433–1452.
Janssen, F., Huettel, M., Witte, U., 2005. Pore-water advection and solute fluxes in permeable marine sediment (II): benthic respiration at three sandy sites with different permeabilities. Limnol. Oceanogr. 50, 779–792.
Jiang, H.-S., Traykovski, P.A., 2006. Direct comparison between numerical simulation and field observation for turbulent flow over large wave orbital scale ripples. Eos Trans. AGU 87 (52) Fall Meet. Suppl., Abstract OS41C-0610.
Kim, W.W., Menon, S., 1999. An unsteady incompressible Navier–Stokes solver for large eddy simulation of turbulent flows. Int. J. Numer. Methods 31, 983–1017.
Laursen, A.E., Seitzinger, S.P., 2002. The role of denitrification in nitrogen removal and carbon mineralization in Mid-Atlantic Bight sediment. Cont. Shelf Res. 22, 1397–1416.
Lohse, L., Kloosterhuis, H.T., van Raaphorst, W., Helder, W., 1996a. Denitrification rates as measured by the isotope pairing method and by the acetylene inhibition technique in continental shelf sediment of the North Sea. Mar. Ecol. Prog. Ser. 132, 169–179.
Lohse, L., Epping, E.H.G., Helder, W., van Raaphorst, W., 1996b. Oxygen pore water profiles in continental shelf sediment of the North Sea: turbulent versus molecular diffusion. Mar. Ecol. Prog. Ser. 145, 63–75.
Meysman, F.J.R., Middelburg, J.J., Herman, P.M.J., Heip, C.H.R., 2003. Reactive transport in surface sediment. II. Media: an object-oriented problem-solving environment for early diagenesis. Comput. Geosci. 29, 301–318.
Meysman, F.J.R., Galaktionov, O.S., Cook, P.L.M., Janssen, F., Huettel, M., Middelburg, J.J., 2007. Quantifying biologically and physically induced flow and tracer dynamics in permeable sediment. Biogeosciences 4, 627–646.
Michael, H.A., Mulligan, A.E., Harvey, C.F., 2005. Seasonal oscillations in water exchange between aquifers and the coastal ocean. Nature 436, 1145–1148.
Middelburg, J.J., Soetaert, K., Herman, P.M.J., Heip, C.H.R., 1996. Denitrification in marine sediment: a model study. Global Biogeochem. Cycles 10, 661–673.
Moore, W.S., 1996. Large groundwater inputs to coastal waters revealed by ^{226}Ra enrichments. Nature 380, 612–614.
Moore, W.S., Shaw, T.J., 1998. Chemical signals from submarine fluid advection onto the continental shelf. Geophys. Res. Lett. 103 (C10), 21,453–21,532.
Moore, W.S., Wilson, A.M., 2005. Advective flow through upper continental shelf driven by storms, buoyancy and submarine groundwater discharge. Earth Planet. Sci. Lett. 235, 564–576.
Ourmieres, Y., Chaplin, J.R., 2004. Visualizations of the disturbed-laminar wave-induced flow above a rippled bed. Exp. Fluids 36, 908–918.
Pope, S.B., 2000. Turbulent Flows. Cambridge University Press, UK.
Precht, E., Huettel, M., 2004. Rapid wave-driven pore water exchange in a permeable coastal sediment. J. Sea Res. 51, 93–107.
Precht, E., Franke, U., Polerecky, L., Huettel, M., 2004. Oxygen dynamics in permeable sediment with wave-driven pore water exchange. Limnol. Oceanogr. 49, 693–705.
Rao, A.M.F., McCarthy, M.J., Gardner, W.S., Jahnke, R.A., 2007. Respiration and denitrification in permeable continental shelf deposits on the South Atlantic Bight: rates of carbon and nitrogen cycling from sediment column experiments. Cont. Shelf Res. 27, 1801–1819.
Reimers, C.E., Stecher, H.A., Taghon, G.L., Fuller, C.M., Huettel, M., Rusch, A., Ryckelynck, N., Wild, C., 2004. In situ measurements of advective solute transport in permeable shelf sands. Cont. Shelf Res. 24, 183–201.
Riedl, R., Huang, N., Machan, R., 1972. The subtidal pump: a mechanism of interstitial water exchange by wave action. Mar. Biol. 13, 210–221.
Shum, K.T., 1992. Wave-induced advective transport below a rippled water–sediment interface. J. Geophys. Res. 97 (C1), 798–808.
Shum, K.T., 1993. The effects of wave induced pore water circulation on the distribution and flux of pore water constituents in a rippled sediment bed. J. Geophys. Res. 98, 10,289–10,301.
Shum, K.T., 1995. A numerical study of the wave-induced solute transport above a rippled bed. J. Fluid Mech. 299, 267–288.
Shum, K.T., Sundby, B., 1996. Organic matter processing in continental shelf sediment — the subtidal pump revisited. Mar. Chem. 53, 81–87.
Soetaert, K., Herman, P.M.J., Middelburg, J.J., 1996. A model of early diagenetic processes from the shelf to abyssal depths. Geochim. Cosmochim. Acta 60, 1019–1040.
Soetaert, K., Middelburg, J.J., Herman, P.M.J., Buis, K., 2000. On the coupling of benthic and pelagic biogeochemical models. Earth-Sci. Rev. 51, 173–201.
Steefel, C.I., DePaolo, D.J., Lichtner, P.C., 2005. Reactive transport modeling: an essential tool and a new research approach for the Earth sciences. Earth Planet Sci. Lett. 240, 539–558.
Thibodeaux, L.J., Boyle, J.D., 1987. Bed form-generated convective-transport in bottom sediment. Nature 325, 341–343.
Traykovski, P., 2007. Observations of wave orbital scale ripples and a nonequilibrium time-dependent model. J. Geophys. Res. 112 (C6) Art. No. C06026.
Van Cappellen, P., Wang, Y., 1996. Cycling of iron and manganese in surface sediment: a general theory for the coupled transport and reaction of carbon, oxygen, nitrogen, sulfur, iron, and manganese. Am. J. Sci. 296, 197–243.
Vance-Harris, C., Ingall, E., 2005. Denitrification pathways and rates in the sandy sediment of the Georgia continental shelf, USA. Geochem. T. 6, 12–18.
Walsh, J.J., 1991. Importance of continental margins in the marine biogeochemical cycling of carbon and nitrogen. Nature 350, 53–55.
Wang, Y.F., Van Cappellen, P., 1996. A multicomponent reactive transport model of early diagenesis: application to redox cycling in coastal marine sediment. Geochim. Cosmochim. Acta 60, 2993–3014.
Webb, J.E., Theodor, J., 1968. Irrigation of submerged marine sands through wave action. Nature 220, 682–683.
Werner, H., Wengle, H., 1991. Large eddy simulation of turbulent flow over and around a cube in a plane channel. Proceedings of Eighth Symposium on Turbulent Shear Flows, Munich, Germany, pp. 1941–1946.
Werner, U., Billerbeck, M., Polerecky, L., Franke, U., Huettel, M., van Beusekom, J.E.E., de Beer, D., 2006. Spatial and temporal patterns of mineralization rates and oxygen distribution in a permeable intertidal sand flat (Sylt, Germany). Limnol. Oceanogr. 51, 2549–2563.
Zedler, E.A., Street, R.L., 2001. Large-eddy simulation of sediment transport: currents over ripples. J. Hydraul. Eng.-ASCE 127, 444–452.
Zedler, E.A., Street, R.L., 2006. Sediment transport over ripples in oscillatory flow. J. Hydraul. Eng.-ASCE 132, 180–193.